



Physics of moderately stretched electrified jets in electrohydrodynamic jet printingAbhishek K. Singh,¹ Anupam Choubey¹,,¹ Rajiv K. Srivastava²,,² and Supreet Singh Bahga^{1,*}¹*Department of Mechanical Engineering, Indian Institute of Technology Delhi, New Delhi 110016, India*²*Department of Textile Technology, Indian Institute of Technology Delhi, New Delhi 110016, India*

(Received 19 October 2022; accepted 23 March 2023; published 13 April 2023)

Electrohydrodynamic (EHD) jet printing involves the deposition of a liquid jet issuing from a needle stretched under the effect of a strong electric field between the needle and a collector plate. Unlike the geometrically independent classical cone-jet observed at low flow rates and high applied electric fields, at a relatively high flow rate and moderate electric field, EHD jets are moderately stretched. Jetting characteristics of such moderately stretched EHD jets differ from the typical cone-jet due to the nonlocalized cone-to-jet transition. Hence, we describe the physics of the moderately stretched EHD jet applicable to the EHD jet printing process through numerical solutions of a quasi-one-dimensional model of the EHD jet and experiments. Through comparison with experimental measurements, we show that our simulations correctly predict the jet shape for varying flow rates and applied potential difference. We present the physical mechanism of inertia-dominated slender EHD jets based on the dominant driving and resisting forces and relevant dimensionless numbers. We show that the slender EHD jet stretches and accelerates primarily due to the balance of driving tangential electric shear and resisting inertia forces in the developed jet region, whereas in the vicinity of the needle, driving charge repulsion and resisting surface tension forces govern the cone shape. The findings of this study can help in operational understanding and better control of the EHD jet printing process.

DOI: [10.1103/PhysRevE.107.045103](https://doi.org/10.1103/PhysRevE.107.045103)**I. INTRODUCTION**

Electrohydrodynamic (EHD) jet printing is a high-resolution direct ink writing (DIW) technique in which an electrified jet of a liquid issuing from a needle is deposited on a motion-controlled substrate [1]. The liquid flowing out from the needle having an outer diameter of $\mathcal{O}(0.1-1\text{ mm})$ stretches and accelerates under the effect of an external electric field of $\mathcal{O}(10^6\text{ V m}^{-1})$ between the needle and the substrate. Although EHD jet printing is derived from the electrospinning process [2], it differs from the latter in the way that the collector substrate is kept relatively very close to the needle to suppress the downstream flow instabilities [3,4]. EHD jet printing has enormous potential for precisely patterning sub-micrometer-scale features suited to a large spectrum of applications such as scaffolds for tissue engineering [5], drug delivery devices [6], printed electronics [7,8], and microfluidic devices [9].

Unlike the conventional DIW process, the EHD jet printing allows patterning a wide range of feature sizes ranging from the needle diameter to as small as two orders of magnitude smaller than the needle diameter, depending on the electric field and flow rate. In the EHD jet printing configuration, stable EHD jetting can occur in three distinct regimes: cone-jet, moderately stretched jet, and thick jet regimes [10]. The cone-jet regime is characterized by a conical meniscus, named the Taylor cone [11], attached to the needle with a fine jet streaming from the tip of the cone. The cone-jet

regime is used to print fine features of $\mathcal{O}(1-10\text{ }\mu\text{m})$. The localized nature of cone-to-jet transition in the cone-jet regime enables jetting characteristics to be independent of the downstream conditions [12]. Therefore, jetting characteristics in the cone-jet regime are identical in both the electrospaying and the EHD jet printing processes despite the differences in the downstream geometrical configuration. The physics of the cone-jet regime has been well described through numerous experimental and numerical studies [12–26]. To this end, experimentally validated full-scale three-dimensional (3D) [19–24], 2D axisymmetric simulations [25,26], and simplified quasi-one-dimensional mathematical models [27,28] have been presented in the literature.

Opposed to the cone-jet regime, the thick jet occurs at a relatively high flow rate and low applied electric field. In the thick jet regime, the jet is negligibly stretched, and its diameter remains approximately equal to the needle diameter. EHD jetting in the moderately stretched jet regime occurs at operating conditions between the cone-jet and the thick jet regimes. The moderately stretched jet is characterized by a slender jet with a gradual cone-to-jet transition. The moderately stretched jet can be used to print features that are relatively broad but finer than the needle diameter. In this work, we focus on the modeling and simulation of the moderately stretched EHD jet applicable in EHD jet printing, where the gap between the needle and substrate is relatively small. This regime is specific to the EHD jet printing process, and corresponding EHD jetting characteristics are not well reported in the literature. Numerical simulations of the slender EHD jets have been reported earlier by Gañán-Calvo [29], Feng [30], and Higuera [31]. However, their simulations are applicable to the

*bahga@mech.iitd.ac.in

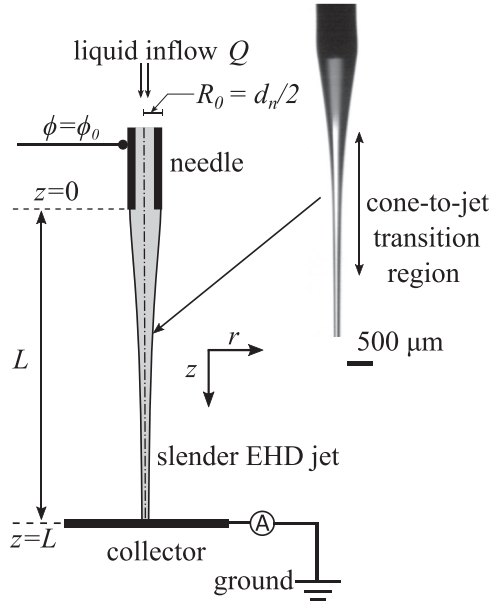


FIG. 1. Schematic illustration of an electrically charged slender jet of a leaky-dielectric liquid. The jet is characterized by an elongated conical meniscus that gradually transitions to a thin jet. The collector substrate is placed relatively close to the metallic needle as opposed to electrospaying.

electrospinning configuration, wherein the needle-to-collector distance is much larger than the cone-to-jet transition region. In contrast, in the present study, the length of the cone-to-jet transition region is comparable to the needle-to-collector distance because, in EHD jet printing, the needle-to-collector distance is significantly smaller. Therefore, the characteristics of moderately stretched slender EHD jets can significantly depend on the downstream conditions.

In this paper, we describe the physics of slender EHD jets observed in near-field EHD jet printing through experimentally validated numerical simulations. The numerical simulations allow predictions of variation of physical quantities such as local electric field, surface charge density, and the conduction and convection current components, which are otherwise impossible to measure in an experiment. Based on the simulation results for varying flow rates and applied electric field, we provide insights into the physical mechanism of moderately stretched EHD jets in EHD jet printing. We begin by discussing the mathematical model and the numerical scheme in Sec. II. Section III presents experiments and the validation of simulation results with the experimental data, Sec. IV describes the EHD jetting behavior using the simulations, and Sec. V gives the concluding remarks.

II. MATHEMATICAL MODELING

We consider a moderately stretched slender EHD jet of a leaky-dielectric liquid flowing out of a needle. The electric field is applied between the needle and the large collector substrate by connecting a high voltage terminal to the metallic needle of outer radius R_0 while grounding the substrate, as shown in Fig. 1. The ground electrode is kept at a distance

L from the needle tip, such that $L/R_0 \lesssim 20$, to suppress the disintegration of the jet into droplets before it impinges on the collector substrate. Leaky-dielectric liquids are conducting enough to ensure quick conduction of charges to the free surface. However, unlike conductors, these liquids also support the tangential electric shear stress that stretches the liquid meniscus and drives the flow in the direction of the electric field [32,33]. Besides the normal and tangential electric stresses on the liquid surface, the jetting behavior is governed by inertia, viscous, capillary, and gravity forces. The net effect of these forces is such that the jet diameter gradually decreases downstream of the needle, as illustrated in Fig. 1. In the presence of an external electric field, charges within the liquid quickly migrate to the free surface and modify the local electric field. The charges migrate to the free surface through conduction, and from there, charges move downstream by surface convection. Therefore, the total current carried by an EHD jet comprises of bulk conduction and surface convection currents. The conduction current dominates near the needle tip, while the surface convection current dominates downstream of the cone-to-jet transition region.

The underlying physics of EHD jets in a needle-plate configuration can be described by performing full-scale 3D or axisymmetric simulations [26]. Besides these methods, quasi-one-dimensional models have also been employed for deriving scaling laws based on the balance between dominant driving and resisting forces [34,35]. However, quasi-1D approximation leads to inaccurate results for the cone-jet regime, wherein the cone transitions to the jet abruptly over a small cone-to-jet transition region with length $L_t \ll d_n$, where d_n is the outer diameter of the needle [36]. Due to the significant disparity in length scales of the cone and the jet, the quasi-1D approximation has been applied separately in the cone and the jet regions to derive the scaling laws for the jet radius and the current carried by the jet [35]. However, as opposed to the cone-jet regime, for moderately stretched EHD jets, the transition length L_t is significantly large and the conical meniscus gradually transitions to a jet. Therefore, the quasi-1D model can directly be used to predict the physical variables of the entire slender EHD jet.

A. Governing equations

We consider a stable and steady jet of a leaky-dielectric liquid having physical properties: density ρ , dynamic viscosity η , interfacial tension γ , electrical conductivity k , and dielectric permittivity ϵ in a dielectric medium of permittivity ϵ_0 and considerably lower density and viscosity. We assume that the jet radius $R = R(z)$ varies gradually along the z direction, and is symmetrical about the centroidal axis of the needle. Under the assumption of fast charge relaxation and momentum diffusion, the EHD jetting under these conditions can be approximated as a quasi-one-dimensional flow problem from the beginning. The steady-state quasi-1D governing equations for mass and momentum conservation and current continuity based on the Taylor-Melcher leaky-dielectric model [33] for an electrified jet of a Newtonian liquid were first presented by Gañán-Calvo [29]. Subsequently, this model was improved by Hohman *et al.* [37,38], and Feng [30] to model the electric field using Coulomb's law. Briefly, these

equations are summarized here. For a steady EHD jet, the conservation of mass and current can be expressed as

$$Q = \pi R^2 v \quad \text{and} \quad (1)$$

$$I = \pi R^2 k E + 2\pi R \sigma v, \quad (2)$$

respectively. Here Q is the constant flow rate, R the jet radius, v the mean axial velocity, I the total current, E the electric field along the center line of the jet, and σ is the surface charge density that can be expressed as $\sigma = \epsilon_0 E_n$, where E_n is the local normal electric field on the jet surface. The first term on the right-hand side of Eq. (2) represents the bulk conduction current I_c , while the second term corresponds to the surface convection current I_s . Note that, for steady EHD jetting, the total current I is invariant of z but depends on the operating flow rate and external electric field.

The momentum conservation equation, which describes the balance of hydrodynamic and electrical forces on the jet, is given as

$$\frac{d}{dz} \left(\frac{\rho v^2}{2} \right) = \rho g + \frac{3}{R^2} \frac{d}{dz} \left(\eta R^2 \frac{dv}{dz} \right) + \frac{2\sigma E}{R} + \frac{d}{dz} \left[\frac{\sigma^2}{2\epsilon_0} - \frac{\gamma}{R} + \frac{\epsilon_0(\epsilon_r - 1)E^2}{2} \right]. \quad (3)$$

Here the left-hand side corresponds to the inertia force per unit volume, and the terms on the right-hand side correspond to the gravity, viscous, tangential electric shear, charge repulsion, interfacial tension, and polarization forces per unit volume, respectively.

Gañán-Calvo [29] proposed a method to determine v , σ , or ($E_n = \sigma/\epsilon_0$) by utilizing the mathematical model described by Eqs. (1)–(3) as a consistent measurement tool. In this approach, Gañán-Calvo used experimentally measured values of $R(z)$ and I to make quantitative measurements of all the remaining variables involved in the EHD jet dynamics, including surface charge density, various force terms, and conduction and convection current components. Later, the same methodology was followed by López-Herrera *et al.* [28] to show the validity of the quasi-1D model for modeling cone-jets. López-Herrera *et al.* [28] used the $R(z)$ and I obtained from 2D numerical simulations as the inputs to the model. The approach of Gañán-Calvo [29] and López-Herrera *et al.* [28] does not provide a self-consistent formulation to calculate all the variables for given operating parameters and boundary conditions, because the electric field is not modelled using Coulomb's law. Instead, the electric field is quantified using the mass, momentum, and charge conservation laws, using measured $R(z)$ and I .

Later, Hohman *et al.* [37,38] modified the simplified quasi-1D model of Gañán-Calvo [29] by separately modeling the electric field using Coulomb's law. The electrostatic potential along the center line of the jet is modelled as a sum of the applied potential between the needle and the collector plate in the absence of the jet and the potential due to an effective line charge density corresponding to free and polarization charges. To approximately satisfy the potential drop between the needle and the collector plate, Hohman *et al.* [38] incorporated the contribution of image charges in the Coulomb's law. Hohman *et al.* [38] also incorporated in their model the

numerically predicted fringe electric field due to the needle protruding the plate-electrode in their setup. However, their model was prone to a ballooning instability and numerically stable solution was obtained for low conductivity liquids when $\sigma(z=0) \approx 0$.

Feng [30] modified the quasi-1D model of Hohman *et al.* [38] by simplifying the integrodifferential equation of the electric field corresponding to the Coulomb's law using an asymptotic approximation of the integral [39]. The simplified equation of the electric field E along the center line of the jet due to total surface charges (free and polarization charge) is expressed as

$$E = E_\infty - \ln \chi \left[\frac{1}{\epsilon_0} \frac{d}{dz} (\sigma R) - \frac{(\epsilon_r - 1)}{2} \frac{d^2}{dz^2} (ER^2) \right], \quad (4)$$

where E_∞ denotes the external electric field in the absence of the jet, $\epsilon_r = \epsilon/\epsilon_0$ is the relative permittivity of the liquid, and $\chi = L/R_0$ is the aspect ratio, L is the needle-to-collector distance and $R_0 = d_n/2$ is the outer radius of the needle. Feng [30] showed that the use of this equation improves the numerical stability. Moreover, the model is insensitive to the inlet boundary condition for the surface charge density, except for a tiny boundary layer near the needle. However, the trade-off is that a constant potential drop across the needle and the collector cannot be enforced. Consequently, the experimentally measured current is required as a model input, instead of the applied potential drop.

Here we follow Feng's approach and model electric field using Eq. (4) and taking experimentally measured current as a model input. Using Eqs. (1)–(4), the four unknowns R , v , σ , and E can be obtained numerically provided that Q and I are known from the experiments. Equations (1)–(4) can be expressed in dimensionless form by nondimensionalizing the physical quantities using the following reference scales:

$$[R, z] = R_0, \quad [v] = \frac{Q}{\pi R_0^2}, \quad [E] = \frac{I}{\pi k R_0^2},$$

$$\text{and } [\sigma] = \frac{\epsilon_0 I}{\pi k R_0^2}. \quad (5)$$

The governing equations (1)–(4) in the dimensionless form are given as

$$\tilde{R}^2 \tilde{v} = 1, \quad (6)$$

$$\tilde{E} \tilde{R}^2 + \text{Pe} \tilde{\sigma} \tilde{R} \tilde{v} = 1, \quad (7)$$

$$\frac{d}{d\tilde{z}} \left(\frac{\tilde{v}^2}{2} \right) - \frac{1}{\text{Fr}} - \frac{3}{\text{Re}} \frac{1}{\tilde{R}^2} \frac{d}{d\tilde{z}} \left(\tilde{R}^2 \frac{d\tilde{v}}{d\tilde{z}} \right) + \frac{1}{\text{We}} \frac{d}{d\tilde{z}} \left(\frac{1}{\tilde{R}} \right) - \mathcal{E} \frac{d}{d\tilde{z}} \left(\frac{\tilde{\sigma}^2}{2} + \beta \frac{\tilde{E}^2}{2} + \frac{2\tilde{\sigma}\tilde{E}}{\tilde{R}} \right) = 0, \quad (8)$$

$$\tilde{E}(\tilde{z}) - \tilde{E}_\infty + \ln \chi \left[\frac{d}{d\tilde{z}} (\tilde{\sigma} \tilde{R}) - \frac{\beta}{2} \frac{d^2}{d\tilde{z}^2} (\tilde{E} \tilde{R}^2) \right] = 0, \quad (9)$$

where the tilde over variable denotes corresponding the nondimensional variable. Here, Pe , Fr , Re , We , β , and \mathcal{E} are

dimensionless group defined as electric Peclet number $Pe = 2\epsilon_0 v_0 / (kR_0)$, Froude number $Fr = v_0^2 / (gR_0)$, Reynolds number $Re = \rho v_0 R_0 / \eta$, Weber number $We = \rho v_0^2 R_0 / \gamma$, electric-to-inertia force $\mathcal{E} = \epsilon_0 E_0^2 / (\rho v_0^2)$, and $\beta = (\epsilon_r - 1)$. Also, note that the total current I is a model parameter, and its experimentally measured value for a given fluid and operating parameters (Q and ϕ) is required as an input by the model.

B. Boundary conditions

The set of two ordinary differential equations (ODEs) Eq. (8) and Eq. (9), along with two algebraic equations (6) and (7) can be solved numerically. These ODEs require four boundary conditions (BCs), one for each \tilde{R} and \tilde{E} at the needle tip and downstream. The jet radius at the tip of the needle is equal to the outer radius of the needle, and hence

$$\tilde{R}(\tilde{z} = 0) = 1. \quad (10)$$

For a one-dimensional slender EHD jet, Feng [30] suggested that the BCs for the electric field at the inlet can be obtained from the charge conservation equation, Eq. (2), provided that the surface charge density is defined at the needle outlet for a given current I . The surface charge density at the needle outlet $\sigma(0)$ primarily depends on the physical properties of the fluid and the overall geometrical configuration; however, finding the exact value of $\sigma(0)$ for a given fluid and geometrical configuration is tedious. Moreover, through numerical simulations, Feng [30] showed that the effect of $\sigma(0)$ is limited to a very small distance $z \lesssim R_0$ in the vicinity of the needle outlet. Consequently, any value of $\sigma(0)$ leads to an identical jet profile outside a tiny boundary layer region [30]. Therefore, we considered $\sigma(0) = 0$, and correspondingly from Eq. (7), the BC for \tilde{E} is

$$\tilde{E}(\tilde{z} = 0) = 1. \quad (11)$$

The downstream BCs for a slender EHD jet in the near-electrode configuration of a needle-plate arrangement can significantly differ from the far electrode needle-plate and the far electrode parallel plate configuration, analyzed earlier by Feng [30] and Higuera [31], respectively. For parallel plate far electrode configuration of slender EHD jet, Feng used $\tilde{E} = \tilde{E}_\infty$ and $\tilde{R}' = -\tilde{R}/4\chi$ at $\tilde{z} = \chi$, which is based on the assumption that the surface convection current is equal to the total current carried by the jet and \tilde{E}_∞ is uniform. However, in the current case, E_∞ varies with z , and both the conduction and the convection currents are relevant downstream of the cone. Therefore, the downstream BCs for modeling electrospinning are not applicable to the moderately stretched jet in an EHD jet printing configuration. The experimental observations of Singh *et al.* [10] shows that the radius of the moderately stretched jet in the inertia-dominated regime attains an asymptotic limit close to the collector plate. Therefore, we use a simplified downstream BC for jet radius as

$$\tilde{R}'(\tilde{z} = \chi) = 0. \quad (12)$$

Our numerical experiments show that the jet profile obtained by considering $\tilde{R}'(\tilde{z} = \chi) = 0$ is almost identical to that obtained from $\tilde{R} + 4\chi\tilde{R}' = 0$. This is because inertia-dominated EHD jets reach an asymptotic radius even over a small

needle-to-collector distance, and the viscous effects due to jet impingement are confined close to the collector.

Beyond the current transfer region, the axial electric field is approximately equal to the external field, $E \approx E_\infty$, during stable EHD jetting [30,31]. The external electric field for a needle-plate configuration can be approximated as the electric field due to two confocal paraboloid surfaces (one as a paraboloid needle and another large paraboloid plate) placed at a distance $z = d_n/4 + L$, here d_n denotes the outer diameter of the needle [10]. Under such assumption, far from the needle tip, the electric field scales as $E_\infty \sim A/z$ along the center line of the needle, where $A = \phi / \ln(2\chi)$. Even numerical simulation in the exact needle and a plate configuration, shown later in Fig. 4, suggests that $E_\infty \sim A/z$. Therefore, we take the fourth BC as

$$\tilde{E} + \chi\tilde{E}' = 0 \quad \text{at } \tilde{z} = \chi. \quad (13)$$

C. Numerical scheme

The mathematical model [Eqs. (6)–(9)] requires dimensionless parameters (Re , We , Fr , Pe , \mathcal{E} , and β) and external electric field E_∞ as the inputs. The dimensionless parameters depend on the physical properties of the liquid, operating parameters, and current carried by the jet I . Hence we used the physical properties, operating parameters, and corresponding measured values of the current I from EHD jetting experiments for all simulations; these experiments are discussed in Sec. III. We computed the external electric field E_∞ in the absence of the jet, corresponding to the exact experimental configuration described in Sec. III. To this end, we performed 2D-axisymmetric simulations using a commercial finite element solver and obtained the axial component of the electric field at $r = 0$ corresponding to different values of the applied electric potential ϕ . The details of the numerical procedure to obtain external electric field E_∞ is discussed in Appendix.

Knowing the values of dimensionless numbers and the external electric field E_∞ , we numerically solved the coupled set of ODEs using boundary value solver `bvp5c` in MATLAB. The `bvp5c` solver requires a good initial guess of the solutions (\tilde{R} and \tilde{E}). We considered an analytical solution of a purely gravity-driven inviscid jet as an initial guess for the jet radius and a linearly varying \tilde{E} as the initial guess for the axial electric field. We slowly ramped the values of \mathcal{E} , which controls the strength of electric forces from zero to the desired value, while using the solution at a particular step as the initial guess for the next step.

III. EXPERIMENTS AND VALIDATION

A. Experimental methodology

The total current I carried by a slender EHD jet depends on the flow rate and the applied potential difference for a given fluid and geometrical configuration [10]. For the same reason, the current carried by a slender jet cannot be considered as an independent variable for modeling the EHD jet using Eqs. (6)–(9). Therefore, to simulate realistic slender EHD jet using the present model, we used the current values measured during the experiments. In particular, we used experimental data of Singh *et al.* [10] for steady jetting of 1-octanol at varying values

TABLE I. The values of the measured current and dimensionless parameters for varying values of flow rate Q and applied potential difference ϕ . The working fluid is 1-octanol, the outer diameter of the needle $d_n = 1$ mm, and aspect ratio $\chi = 20$.

Q (ml min ⁻¹)	ϕ (kV)	I (nA)	Re	We $\times 10^{-2}$	Fr	Pe $\times 10^{-4}$	\mathcal{E} $\times 10^{-3}$
3.0	4.8	108.8	3.3	7.6	0.83	5.55	3.1
3.0	5.2	113.8	3.3	7.6	0.83	5.55	3.4
3.0	5.6	120.2	3.3	7.6	0.83	5.55	3.8
3.0	6.0	127.0	3.3	7.6	0.83	5.55	4.2
2.5	4.8	101.3	2.7	5.3	0.57	4.63	3.8
3.0	4.8	110.4	3.3	7.6	0.83	5.55	3.1
4.0	4.8	130.8	4.4	13.5	1.47	7.40	2.5
5.0	4.8	151.9	5.5	21.1	2.29	9.26	2.2

of applied potential ϕ at a fixed Q . In these experiments, jetting is dominated by inertia and the effect of polarization are negligible [10]. The jetting in this regime occurs under the following condition as suggested by Gañán-Calvo [35],

$$\frac{Q}{Q_0} \gg \left(\frac{1}{\text{Re}_0} \frac{Q}{Q_0} \right)^{1/4} \text{ and } \left(\frac{1}{\beta} \frac{Q}{Q_0} \right) \gg 1, \quad (14)$$

where the characteristics flow rate $Q_0 = (\gamma\epsilon_0/\rho k)$ and electric Reynolds number $\text{Re}_0 = [\rho\epsilon_0\gamma^2/(k\eta^3)]^{1/3}$. We used the current data at $Q = 3$ ml min⁻¹ and $\chi = 20$ for varying potential difference. The physical properties of 1-octanol are $\rho = 825.5$ kg m⁻³, $\eta = 8$ mPa s, $\gamma = 26$ mN m⁻¹, $k = 4.05$ $\mu\text{S m}^{-1}$, and $\epsilon = 9.15 \times 10^{-11}$ F m⁻¹. In these experiments, $Q/Q_0 \sim \mathcal{O}(100)$, $\text{Re}_0 \sim \mathcal{O}(1)$, and $\beta = 10.3$, therefore, the condition for dominant inertia and negligible polarization forces given by Eq. (14) is satisfied. Table I presents values of the total current I and dimensionless numbers corresponding to the varying values of ϕ taken from Singh *et al.* [10].

In addition to the experimental data from the literature, we performed experiments for varying flow rates, $Q = 2.5$ ml min⁻¹ to $Q = 5.0$ ml min⁻¹ at constant ϕ with 1-octanol. We used the same experimental setup and followed the similar methodology as Singh *et al.* [10]. Briefly, the experimental setup consisted of a 35-mm-long metallic needle having an inner diameter of 0.66 mm and an outer diameter of 1.0 mm placed perpendicular to a 50-mm-diameter circular collector disk at a distance 10 mm from the needle tip. We applied a fixed potential $\phi = 4.8$ kV on the metallic needle and grounded the collector substrate. The working liquid was pumped through the needle using a syringe pump (KD Scientific, Legato 180). We visualized the jet through a stereo-microscope (Radical Scientific, 8 – 50 \times zoom) equipped with a camera. We captured the snapshots of the jet using the camera and simultaneously measured the current carried by the jet through a laboratory-made current measuring setup. Table I presents the values of the measured currents at $\phi = 4.8$ kV and for varying flow rates, and the corresponding dimensionless parameters.

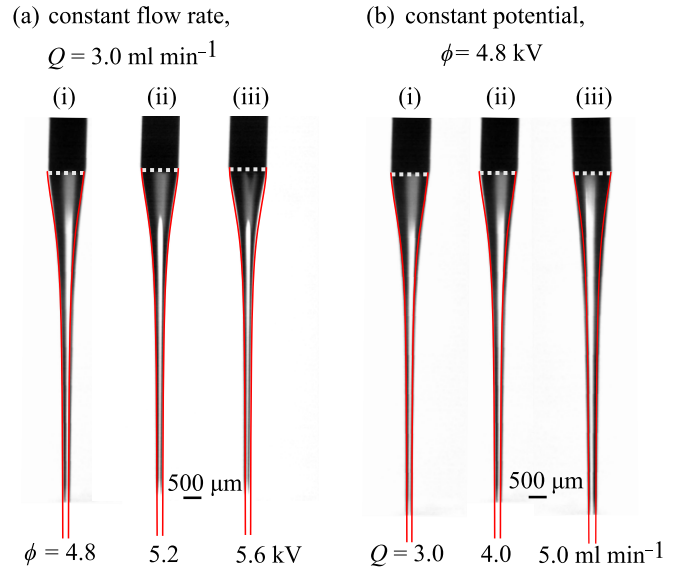


FIG. 2. Comparison of jet profiles measured in the experiments and predicted by numerical simulations (a) for constant flow rate $Q = 3.0$ ml min⁻¹ at three values of applied potential: (i) $\phi = 4.8$ kV, (ii) $\phi = 5.2$ kV, and (iii) $\phi = 5.6$ kV, and (b) for constant applied potential $\phi = 4.8$ kV at three different values of flow rate: (i) $Q = 3.0$ ml min⁻¹, (ii) $Q = 4.0$ ml min⁻¹, and (iii) $Q = 5.0$ ml min⁻¹. Numerically predicted jet profiles agree well with the experimental observations for varying values of Q and ϕ .

B. Experimental validation

Figure 2 shows the comparison of simulated and measured steady-state jet profiles at varying values of Q and ϕ . The red lines show the simulated jet profiles overlaid on the corresponding snapshots of the jet obtained from the experiments. In particular, Fig. 2 shows a comparison of six different cases grouped into two categories, one at a constant $Q = 3.0$ ml min⁻¹ and varying ϕ as shown in Fig. 2(a) and another at a constant $\phi = 4.8$ kV and varying Q as shown in Fig. 2(b). This figure shows that the jet profiles obtained from the numerical simulations agree well with the experimental jet shape. However, there is a small but noticeable deviation in the predicted jet profile at a high flow rate ($Q = 5.0$ ml min⁻¹ and $\phi = 4.8$ kV) close to the needle as shown in Fig. 2(b)(iii). For the remaining cases shown in Fig. 2, the agreement between the simulations and the experiments is excellent. The discrepancy in the prediction of jet shapes is primarily due to two main reasons. First, the asymptotic approximation of the Coulomb's law, Eq. (4), has a higher deviation from the exact equation for electric field near the domain boundaries. Second, as explained in Appendix, the fringe electric field at needle tip is 3D in nature which is only approximately incorporated in the quasi-1D model through E_∞ . Despite these approximations, our model shows a maximum of 10% deviation in the predictions of the jet radius from the experiments, which is a reasonably good prediction considering the simplicity of the model. Therefore, this experimentally validated model can be confidently used to estimate the spatial variation in various physical properties of a slender EHD jet, such as local electric field, free surface charge density, various current components, and the magnitudes of different

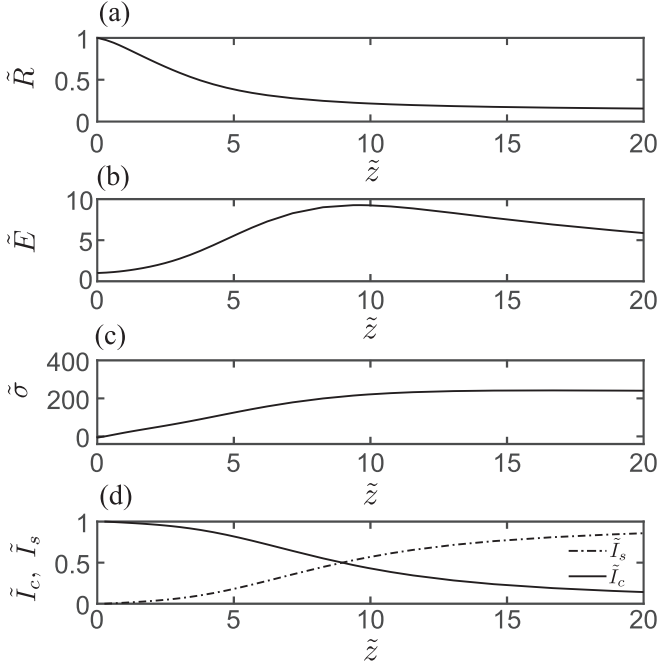


FIG. 3. Axial variation of simulated dimensionless physical variables from the needle tip to collector plate: (a) jet radius \tilde{R} , (b) local electric field \tilde{E} , (c) surface charge density $\tilde{\sigma}$, and (d) individual components of the total current: conduction current $\tilde{I}_c = \tilde{E}\tilde{R}^2$ and surface convection current $\tilde{I}_s = \text{Pe}\tilde{R}\tilde{\sigma}\tilde{v}$. This simulation was performed for $\text{Re} = 3.3$, $\text{We} = 7.6 \times 10^{-2}$, $\text{Fr} = 0.83$, $\text{Pe} = 5.55 \times 10^{-4}$, and $\mathcal{E} = 3.1 \times 10^{-3}$ corresponding to $Q = 3.0 \text{ ml min}^{-1}$ and $\phi = 4.8 \text{ kV}$. The jet radius gradually decreases toward the collector substrate. The conduction current does not completely convert to convection current downstream. Additionally, the jet properties vary smoothly over the entire jet path.

force terms, which otherwise cannot be directly measured in experiments.

IV. RESULTS AND DISCUSSION

Having validated the simulations with the experiments, we now present the axial variation of the physical properties of the jet from the needle tip to the collector plate. Figure 3 shows the axial variation of the dimensionless jet radius \tilde{R} , local electric field \tilde{E} , surface charge density $\tilde{\sigma}$, and components of the current: conduction current $\tilde{I}_c = \tilde{E}\tilde{R}^2$ and surface convection current $\tilde{I}_s = \text{Pe}\tilde{\sigma}\tilde{R}\tilde{v}$, respectively at $\text{Re} = 3.3$, $\text{We} = 7.6 \times 10^{-2}$, $\text{Fr} = 0.83$, $\text{Pe} = 5.55 \times 10^{-4}$, and $\mathcal{E} = 3.1 \times 10^{-3}$ corresponding to $Q = 3.0 \text{ ml min}^{-1}$ and $\phi = 4.8 \text{ kV}$. Figure 3 shows that the jet radius decreases faster near the needle tip and almost attains an asymptotic value downstream. The axial electric field gradually rises to a peak value and then smoothly relaxes downstream. The surface charge density increases gradually along the flow direction and then remains nearly constant throughout the jet path. Because \tilde{R} , $\tilde{\sigma}$, and \tilde{E} are related through the charge conservation equation Eq. (7), slow variations of \tilde{R} and $\tilde{\sigma}$ induce a gradual variation of \tilde{E} . Figure 3(d) shows the axial variation of the dimensionless bulk conduction and surface convection currents. The total current carried by the jet is primarily due to

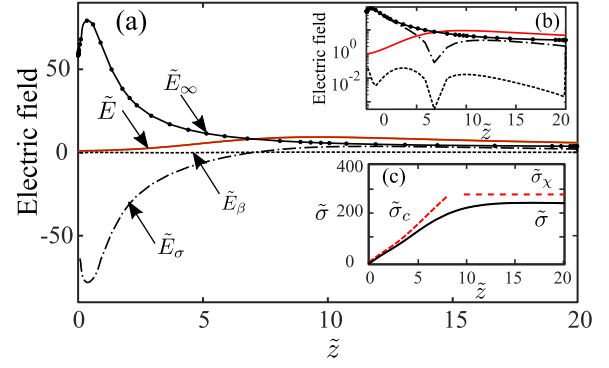


FIG. 4. Various contributions to the axial electric field. The same data is replotted in inset (b) on a semilog plot to show the relative magnitude of various contributions of the axial electric field. The electric field due to polarization charges is negligibly small, $\tilde{E}_\beta = \ln \chi (\beta/2)d^2(\tilde{E}\tilde{R}^2)/d\tilde{z}^2 \approx \mathcal{O}(10^{-2})$, and the electric field due to free surface charges approximately balances the external electric field \tilde{E}_∞ in the elongated conical meniscus where $\tilde{R} \sim \mathcal{O}(1)$. In the inset (c), the approximations of the charge density near the cone $\tilde{\sigma}_c \approx \int \tilde{E}_\infty d\tilde{z}/(\ln \chi \tilde{R})$ and far downstream ($\tilde{z} \sim \chi$), $\tilde{\sigma}_\chi = \tilde{R}/\text{Pe}$, are plotted along with the $\tilde{\sigma}$ obtained from the charge conservation Eq. (7). Close to the needle tip, $\tilde{\sigma} \approx \tilde{\sigma}_c$, which suggests that the surface charges develop such that the external electric field does not penetrate into the liquid meniscus close to the needle tip.

the conduction current in the elongated conical meniscus near the needle outlet. The conduction current gradually decreases while the surface convection current monotonically increases downstream. Although the surface convection current \tilde{I}_s increases at the expense of the conduction current (\tilde{I}_c), \tilde{I}_c does not completely transform to \tilde{I}_s downstream of the conical meniscus. The profiles of $\tilde{\sigma}$, \tilde{E} , \tilde{I}_c , and \tilde{I}_s of the slender EHD jet significantly differ from the cone-jet, wherein $\tilde{\sigma}$ and \tilde{E} shoot to their peak values and then relax downstream within a relatively narrower region close to cone tip [22,23]. Moreover, in a cone-jet, the conduction current entirely converts to the convection current across the current transfer region, which lies at two to five radial distances from the needle tip downstream [22,23].

Figure 4(a) shows the axial variation of various contributions to the axial electric field \tilde{E} in Eq. (9). Shown in Fig. 4 are the net axial electric field \tilde{E} , external electric field \tilde{E}_∞ , electric field due to free surface charges $\tilde{E}_\sigma = -\ln \chi d(\tilde{\sigma}\tilde{R})/d\tilde{z}$, and that due to the polarization charges $\tilde{E}_\beta = \ln \chi (\beta/2)d^2(\tilde{E}\tilde{R}^2)/d\tilde{z}^2$. The external electric field due to applied potential ϕ is of form A/\tilde{z} , except at the needle outlet, where A is a constant that depends on the applied potential ϕ . From Fig. 4(a), we notice that the local electric field \tilde{E} gradually increases close to the needle, surpasses the external field in the intermediate region, and approaches the external field \tilde{E}_∞ , downstream where jet attains an asymptotic limit. To compare the order-of-magnitude of various contributions to the overall electric field, \tilde{E} , \tilde{E}_∞ , \tilde{E}_σ , and \tilde{E}_β are plotted on a semilog plot in Fig. 4(b). The polarization field \tilde{E}_β is negligibly small throughout the jet as shown in Fig. 4(b). Moreover, the electric field due to free charges completely counteracts the external electric field in the vicinity of the needle tip. In the conical meniscus region where $\tilde{R} \sim \mathcal{O}(1)$, the

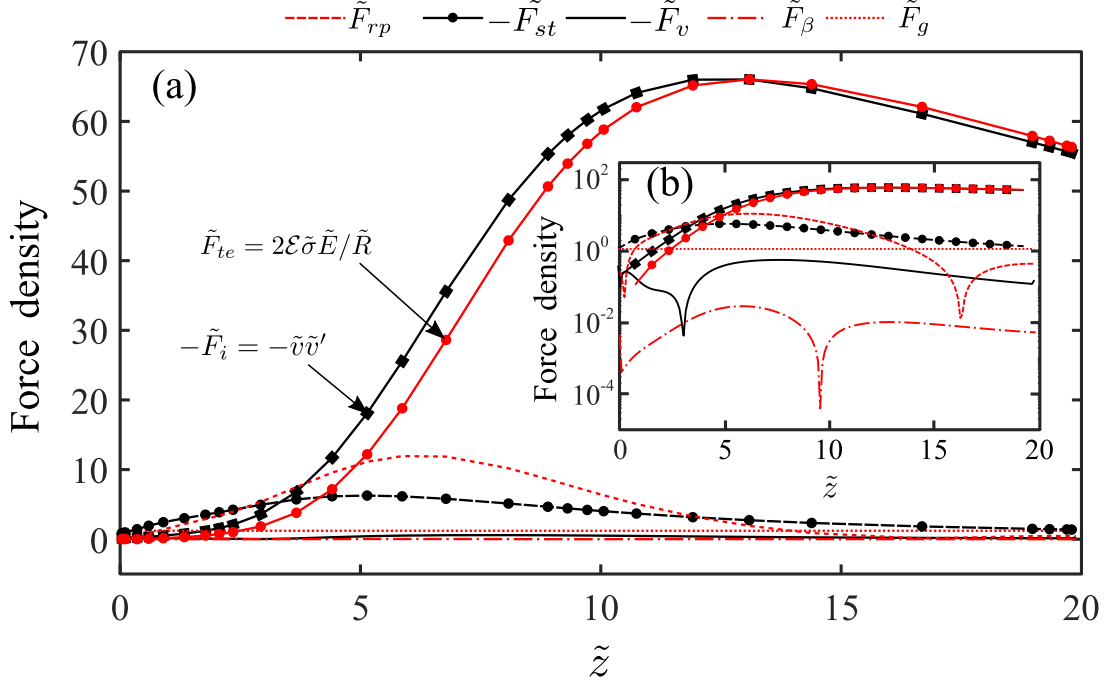


FIG. 5. Axial variation of various forces governing the steady EHD jetting. (a) The force densities in momentum equation [Eq. (8)] are evaluated for $\text{Re} = 3.3$, $\text{We} = 7.6 \times 10^{-2}$, $\text{Fr} = 0.83$, $\text{Pe} = 5.55 \times 10^{-4}$, and $\mathcal{E} = 3.1 \times 10^{-3}$ corresponding to $Q = 3.0 \text{ ml min}^{-1}$ and $\phi = 4.8 \text{ kV}$. The sign of resisting forces have been reversed for easy comparison with the driving forces. In the inset, (b) the absolute value of the forces are replotted on the semilog plot. The inertia force \tilde{F}_i and tangential electric force \tilde{F}_{te} are significantly larger than all other forces throughout the jet except in the vicinity of the needle tip, where interfacial tension force \tilde{F}_{st} approximately balances the free charge repulsion force \tilde{F}_{rp} .

charges develop on the surface in such a way that the external field does not penetrate the meniscus. In this region, the local electric field is equal to the field necessary to carry the total current, $\tilde{E} \approx 1/\tilde{R}^2$. To show that $\tilde{E}_\sigma \approx \tilde{E}_\infty$ in the vicinity of the needle tip, we note that close to the needle $\tilde{E}_\beta \ll \tilde{E}_\infty$ and $\tilde{E} \approx 1/\tilde{R}^2 \ll \tilde{E}_\infty$. Therefore, the surface charge density near the needle tip can be approximated as using Eq. (9),

$$\tilde{\sigma}_c = \frac{1}{\ln \chi \tilde{R}(z)} \int_0^z \tilde{E}_\infty(\xi) d\xi. \quad (15)$$

The approximate value of surface charge density $\tilde{\sigma}_c$ is plotted along with the simulated surface charge density $\tilde{\sigma}$ in the inset of Fig. 4. From Fig. 4(c), we observe that $\tilde{\sigma} \approx \tilde{\sigma}_c$ in the vicinity of the needle, where $\tilde{R} \sim \mathcal{O}(1)$. However, downstream, the approximated surface charge density ($\tilde{\sigma}_c$) deviates from the actual ($\tilde{\sigma}$) because \tilde{E} is no longer negligible compared with \tilde{E}_∞ . Physically, as the jet cross section decreases downstream, the resistance to axial charge conduction increases. Hence, the charges must be carried through the surface convection to ensure the continuity of the current. Therefore, the surface charge density surges due to lower jet speed in the elongated conical meniscus. However, downstream, $\tilde{\sigma}$ approaches an asymptotic limit when $\tilde{R}' \rightarrow 0$ and $\tilde{E} \rightarrow \tilde{E}_\infty$. Downstream, the order of magnitude of the surface charge density can be estimated from the fact that the surface convection current approaches the total current, hence at $\tilde{z} = \chi$, $\tilde{I}_s \approx 1$ and the surface charge density $\tilde{\sigma}$ approaches \tilde{R}/Pe as shown in Fig. 4(c).

Next, to describe the physics of slender EHD jet, we estimate individual force terms in the momentum equation (8).

The various forces that govern the EHD jetting phenomenon can be grouped into driving and resisting forces, and are plotted in Fig. 5(a). In addition, to clearly distinguish the order-of-magnitude of various forces, these forces are replotted on a semilog plot in Fig. 5(b). The driving forces stretch the jet while the resisting forces oppose the jet's stretching. The force due to gravity force $\tilde{F}_g = 1/\text{Fr}$, tangential electric force $\tilde{F}_{te} = 2\mathcal{E}\tilde{\sigma}\tilde{E}/\tilde{R}$, and free charge repulsion force $\tilde{F}_{rp} = \mathcal{E}\tilde{\sigma}\tilde{\sigma}'$ stretch the jet, whereas inertia force $\tilde{F}_i = \tilde{v}\tilde{v}'$, viscous force $\tilde{F}_v = 3(\tilde{R}^2\tilde{v}')/(\text{Re}\tilde{R}^2)$, and interfacial tension force $\tilde{F}_{st} = (1/\text{We}\tilde{R})'$ resist the jet's stretching; here prime over the variables represents the derivative of the corresponding variable with respect to axial distance z . Moreover, the polarization force $\tilde{F}_\beta = \mathcal{E}\beta\tilde{E}\tilde{E}'$ can stretch or resist the stretching of the jet depending on the axial location. From Fig. 5(b), we observe that the inertia and tangential electric forces are dominant forces, charge repulsion and surface tension forces are subdominant forces, and gravity, viscous, and polarization forces are negligibly small. We also note that \tilde{F}_i and \tilde{F}_{te} are small near the needle tip compared to \tilde{F}_{rp} and \tilde{F}_{st} , suggesting that the elongated conical meniscus results from the balance of surface tension and charge repulsion forces. However, for $\tilde{z} \gtrsim 5$, where the jet is significantly stretched, \tilde{F}_i and \tilde{F}_{te} exceed all other forces. This suggests that the downstream EHD jetting is governed by the balance of inertia and tangential electric forces. Besides the tangential electric force, free charge repulsion force also contributes to the jet's stretching in the intermediate region, $5 \lesssim \tilde{z} \lesssim 10$. Moreover, in the intermediate region, surface tension \tilde{F}_{st} resists the jet's stretching.

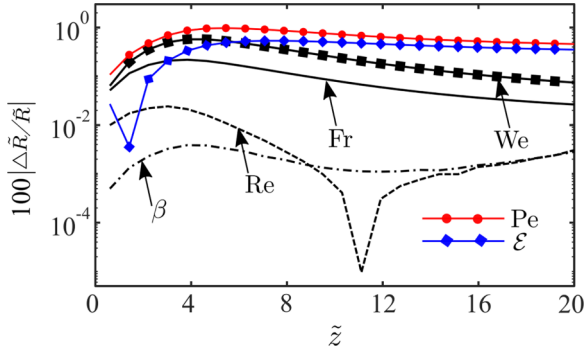


FIG. 6. Sensitivity of the jet radius. Axial variation of the relative change in the jet radius corresponding to a 1% change in the various dimensionless model input parameters has been plotted. The reference values of dimensionless numbers are: $Re = 3.3$, $We = 7.6 \times 10^{-2}$, $Fr = 0.83$, $Pe = 5.55 \times 10^{-4}$, and $\mathcal{E} = 3.1 \times 10^{-3}$. The jet radius is most sensitive to the Pe and \mathcal{E} .

A. Sensitivity analysis

The nondimensional governing Eqs. (6)–(9) suggest that the EHD jetting is governed by the following dimensionless numbers: Reynolds number Re , Weber number We , Froude number Fr , electrical Peclet number Pe , electric-to-inertia force \mathcal{E} , and permittivity ratio β . However, EHD jetting behavior is not sensitive to all these dimensionless numbers. Therefore, we performed sensitivity analysis to identify the dimensionless model parameters that significantly affect the jet characteristics. To this end, we individually perturbed the value of each dimensionless model parameter and evaluated their effect on the predicted jet radius by computing the corresponding fractional change in the radius $|\Delta\tilde{R}/\tilde{R}| \times 100\%$. The sensitivity analysis was performed for the same parameter corresponding to Figs. 3–5. That is, at $Re = 3.3$, $We = 7.6 \times 10^{-2}$, $Fr = 0.83$, $Pe = 5.55 \times 10^{-4}$, and $\mathcal{E} = 3.1 \times 10^{-3}$ for $Q = 3.0 \text{ ml min}^{-1}$ and $\phi = 4.8 \text{ kV}$.

Figure 6 shows the axial variation of the relative change in the jet radius on perturbing the individual dimensionless parameters. This figure shows that the fractional change in the jet radius is most sensitive to Pe , \mathcal{E} , and We . Other dimensionless parameters (Fr , Re , and β) have a considerably lower effect on the jet radius because the gravity, viscous, and polarization force terms are negligibly small in the moderately stretched jet of 1-octanol. Additionally, we also notice that the jet radius is primarily sensitive to Pe and \mathcal{E} far downstream. The Peclet number governs the amount of charge on the jet surface, and \mathcal{E} governs the relative strength of the dominant electric and inertia forces. For the same reason, the asymptotic jet radius or diameter depends primarily on Pe and \mathcal{E} .

B. Effect of flow rate and applied potential

Having described the effect of relevant forces and dimensionless numbers on the moderately stretched EHD jet, we now discuss the effect of flow rate and potential difference on the jetting behavior, which are the primary operating parameters in EHD jetting. The stable EHD jetting occurs for a wide range of flow rates but a narrow range of the applied potential [10,13]. We present the simulation results for two cases: (i)

for varying Q at fixed $\phi = 4.8 \text{ kV}$ and (ii) for varying ϕ at fixed flow rate $Q = 3.0 \text{ ml min}^{-1}$. Note that the total current I also varies with Q and ϕ as shown in Table I. Hence, the reference scales for the local electric field $I/\pi kR_0^2$ and the surface charge density $\epsilon_0 I/\pi kR_0^2$ vary on varying Q and ϕ . Consequently, dimensionless numbers dependent on I also vary on varying the ϕ and Q . Therefore, for comparing the jetting behavior at varying Q and ϕ (and hence I), hereafter all physical quantities are presented in their dimensional form.

1. Effect of flow rate

Figure 7 shows the axial variation of R , σ , E , I_c/I , and I_s/I at four different flow rates, $Q = 2.5, 3.0, 4.0,$ and 5.0 ml min^{-1} . Figure 7(a) shows that the jet thickens on increasing the flow rate, except close to the needle, $z/R_0 \lesssim 5$, where the jet radius does not vary significantly. This is because, for $z/R_0 \lesssim 5$, the elongated cone shape is governed by the balance of interfacial tension and charge repulsion forces, which do not depend on the flow rate. In contrast, for $z/R_0 \gtrsim 5$, the jet stretches due to the balance of inertia and tangential electric forces. In particular the radius of the jet near the collector $R(z=L)/R_0 \sim Q$ as shown in the inset of Fig. 7(a). This is consistent with the experimentally observed scaling of jet radius for moderately stretched jet reported by Singh *et al.* [10]. The ratio of the tangential electric force to the inertia force is represented by the dimensionless electric-to-inertia force $\mathcal{E} = \epsilon_0 E_0^2/\rho v_0^2 \sim I^2/Q^2$. As shown in Table I, the dimensionless electric-to-inertia force \mathcal{E} decreases with increasing Q at a fixed ϕ . Therefore, the strength of tangential stretching forces decreases compared with the inertia as Q increases, resulting in a thicker jet at higher Q .

Figure 7(b) shows the axial variation of surface charge density σ for varying Q . From Fig. 7(b), we notice that the surface charge density σ varies marginally with Q . An insignificant change in surface charge density throughout the jet can be understood by considering approximations of σ at two extreme axial locations, one near the needle tip and the other far downstream. From Eq. (15), the charge density near the needle tip can be approximated as $\sigma \approx \int \epsilon_0 E_\infty dz/R \ln(L/R_0)$. Because E_∞ is independent of Q , and R does not vary much with Q near the needle tip, σ varies marginally with Q . Near the collector plate, the convection current tends to the total current, hence the surface charge density can be approximated as $\sigma \approx I/\pi Rv$, as shown in Fig. 4(b). From the simulation results, we found that the maximum variation in downstream jet velocity v is approximately 5% for all cases, and both I and R increase almost in the same proportion. In particular, a thicker jet at a higher flow rate offers lesser conduction resistance. Then correspondingly increase in I offsets increase in R and $\sigma \approx I/Rv$, leading to a marginal change in σ .

Next, we present the effect of varying Q on the axial electric field as a function of z in Fig. 7(c). The electric field decreases with Q in the intermediate region $5 \lesssim z/R_0 \lesssim 10$. However, the flow rate has little effect on the local electric field in the region where $R \sim \mathcal{O}(1)$ and far downstream. Close to the needle tip ($z/R_0 \lesssim 5$), $I_c \approx I$, and hence the electric field $E \approx I/k\pi R^2 \sim I/R^2$. Because $R/R_0 \sim \mathcal{O}(1)$ varies negligibly with Q near the needle tip and the $E \sim I$, the local

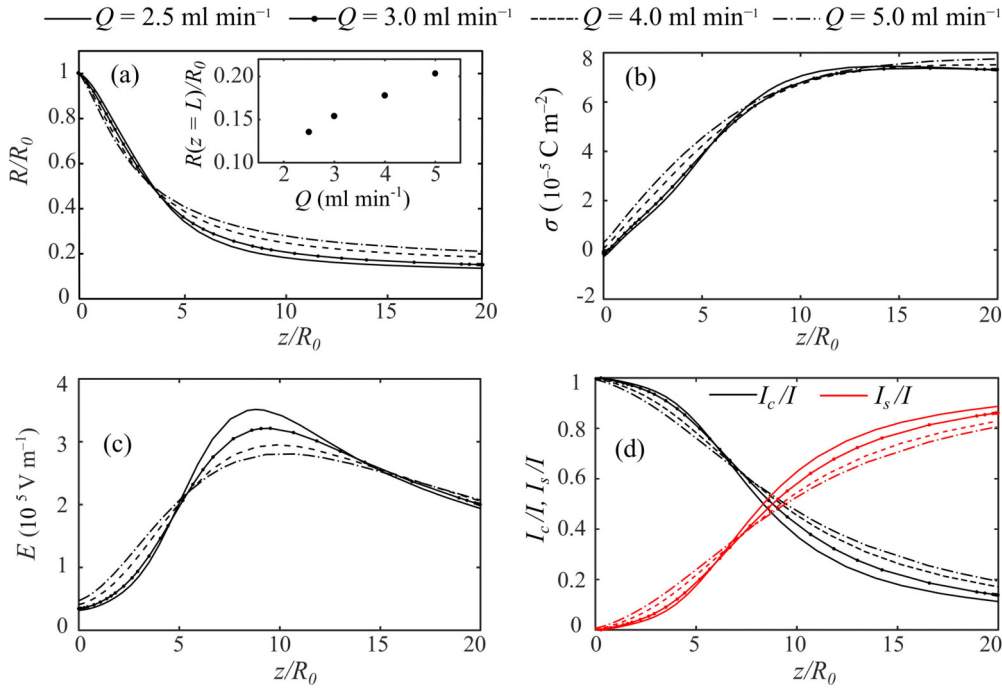


FIG. 7. Physical properties of the slender EHD jet at varying Q at $\phi = 4.8$ kV: (a) jet radius R , (b) surface charge density σ , (c) electric field E , and (d) fraction of the conduction current I_c/I and the convection current I_s/I . The jet thickens on increasing the flow rate, and the asymptotic jet radius scales as $R/R_0 \sim Q$, as shown in the inset of (a). The surface charge density is relatively invariant of the flow rate. Close to extreme ends, E is higher at higher Q . However, in the cone region $z/R_0 \lesssim 5$, E decreases with increasing Q . The fraction of the conduction current increases with increasing flow rate while the fraction of the convection current behaves oppositely.

electric field E increases with I , and hence with Q , which can be seen in Fig. 7(c). In the asymptotic jet region ($z/R_0 \gtrsim 10$), the local electric field is independent of the flow rate because E approaches E_∞ downstream, and the external electric field E_∞ does not vary with Q . In the intermediate region, the elongation of the meniscus intensifies the local electric field due to the surge of surface charge density σ . Finally, Fig. 7(d) shows that the fraction of conduction current increases while convection current decreases with Q because a thicker jet at higher Q offers lesser resistance to charge conduction, resulting in a higher fraction of conduction current.

2. Effect of applied potential

Next, we discuss the effect of varying potential difference ϕ on the behavior of the slender EHD jet. Figures 8(a)–8(d) show the axial variation of R , σ , E , I_c/I , and I_s/I at four different values of applied potential, $\phi = 4.8, 5.2, 5.6,$ and 6.0 kV at a fixed flow rate $Q = 3.0$ ml min $^{-1}$. The higher potential difference leads to greater stretching of the jet and, consequently, a thinner jet at higher ϕ . The effect of ϕ on the downstream behavior of the jet is the opposite of that of the flow rate because increasing ϕ leads to an increase in the driving tangential force F_{te} , whereas increasing Q increases the resisting inertia force F_i . Therefore, as the jet thins at higher ϕ , the fraction of the conduction current decreases while the convection current increases with ϕ , as can be seen from Fig. 8(d), in order to maintain the total current I . The surface charge density in the asymptotic jet region scales as $\sigma \sim I_c Q/R \sim IQ/R$. Since $R \sim Q$ and I increases with ϕ , σ increases with an increase in ϕ as observed in Fig. 8(b).

Figure 8(c) shows the variation of the axial electric field as a function of z . From Fig. 8(c), we notice that the local electric field E increases with ϕ from the needle tip to the collector plate. However, increase in E is relatively negligible in the vicinity of the needle tip and maximum in the intermediate region where jet stretching is most significant. Despite the increase in ϕ and E_∞ , E changes marginally in the cone region because the charges on the cone surface completely screen the local electric field, as shown in Fig. 4. In the intermediate region, the jet stretching intensifies the local electric field, and the jet stretches more at higher ϕ ; hence E increases with ϕ in this region. Downstream, where $E \sim E_\infty$, the axial electric field increases with ϕ due to an increase in E_∞ .

V. CONCLUSIONS

We have described the physics of moderately stretched slender EHD jets observed in the EHD jet printing process. Such EHD jets form at a relatively high flow rate and moderate electric potential. Unlike the classical cone-jet, which has a very localized cone-to-jet transition, the length of the cone-to-jet transition region for a moderately stretched jet is the order of the needle-to-collector distance. As opposed to the cone-jets, the moderately stretched jet's characteristics depend on the geometrical configuration.

In this work, we have considered inertia-dominated moderately stretched EHD jet issuing from a long metallic needle held close to the collector under a strong electric field. To describe the physics of the jet, we have used a quasi-one-dimensional leaky-dielectric jet model with boundary

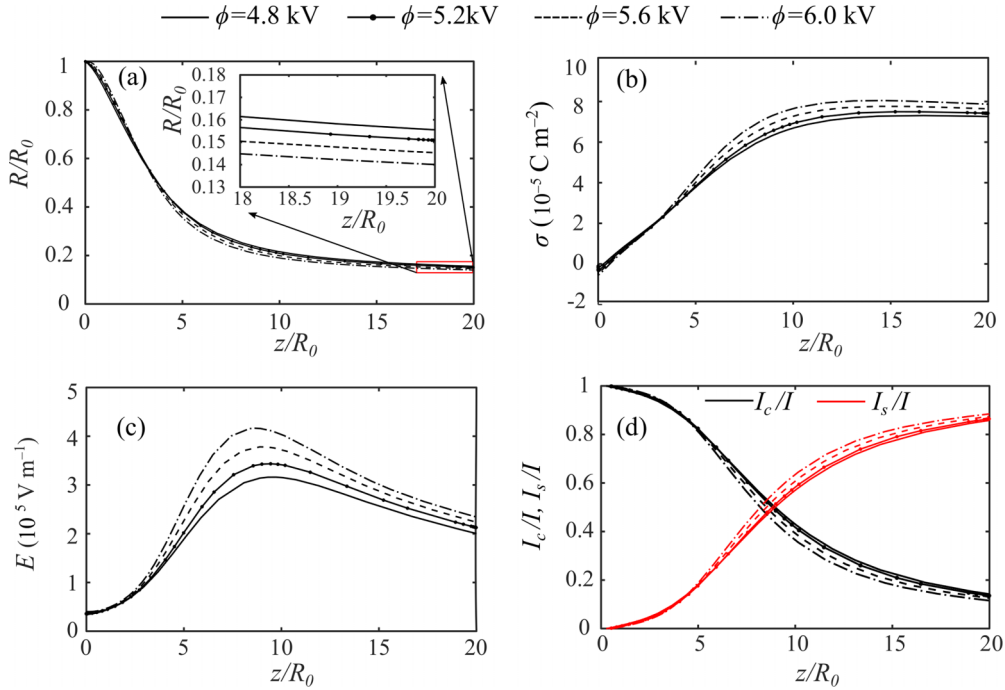


FIG. 8. Jet characteristics for varying ϕ at $Q = 3.0 \text{ ml min}^{-1}$: (a) jet radius R , (b) surface charge density σ , (c) electric field E , and (d) fraction of the conduction current I_c/I and the convection current I_s/I . The jet stretches more with increasing ϕ . In addition, the surface charge density and the local electric field increase with ϕ except close to the needle tip. The fraction of conduction current decreases while the convection current increases with ϕ .

conditions relevant to the EHD jet printing process. We have presented detailed experimental validations of numerical simulation for varying process parameters. After that, we have explained the underlying physics of slender EHD jets based on numerically predicted physical quantities. The stretching of the jet is governed by the inertia and tangential electric shear forces in the developed jet region, whereas the jet shape is governed by the surface tension and charge repulsion forces near the tip of the needle. Through simulations, we showed that, unlike the cone-jets, at moderate jet stretching, the conduction current does not completely convert to convection current downstream. Furthermore, using simulations, we have also discussed the dynamics of slender EHD jets for varying process parameters by examining physical quantities, such as jet radius, surface charge density, local electric field, and conduction and convection currents. The physical understanding of the inertia-dominated moderately stretched EHD jets described here can be helpful for the design, performance monitoring, and control of EHD jet printing.

In the current work, we focused on the EHD jetting caused by dominant inertia and tangential electric forces. Although the bulk of liquids display EHD jetting dominated by inertia and tangential electric forces, some other liquids may exhibit jetting where viscous and polarization forces dominate. Applying the current methodology to examine jetting of moderately stretched EHD jet applicable to EHD jet printing configuration for liquids with dominant viscous and polarization forces would be a logical extension of the current research. Similarly, the simulation approach presented here can be extended in the future for modeling non-Newtonian liquids.

ACKNOWLEDGMENTS

We acknowledge the financial support received from the Science and Engineering Research Board (SERB), Government of India, under the Core Research Grant scheme (Grant No. CRG/2022/002148) and the Mathematical Research Impact Centric Support (MATRICS) scheme (Grant No. MTR/2022/000080). The authors have no conflicts to disclose. The data that support the findings of this study are available within the article.

APPENDIX: FRINGE FIELD

The fringe electric field near the needle tip is three-dimensional in nature [38]. To accommodate this nonuniform 3D electric field in the quasi-1D mathematical model, we use numerically computed the external electric field $E_\infty(z)$ in Eq. (4). To this end, we performed full-scale numerical simulations using a commercial finite element solver to obtain the external electric field between the needle and the collector plate in the absence of the jet. We used a computational domain replicating the exact experimental setup described in the experimental section. We solved Laplace equation, $\nabla^2\phi = 0$, in the domain with the boundary conditions: $\phi = \phi_0$ at the needle, $\phi = 0$ at the collector plate, and insulated far-away boundaries. We discretized the computational domain using a triangular mesh and performed grid dependency tests to obtain an accurate solution. Figure 9(a) shows that the electric field is 3D in nature close to the needle, whereas beyond few radial distances from the needle, the field points along the axial direction. Figure 9(b) shows the corresponding variation of

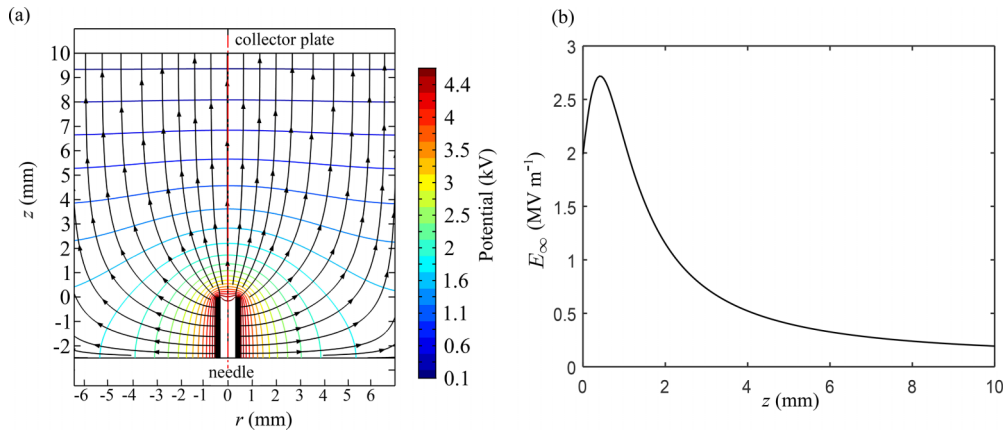


FIG. 9. Simulated electric field distribution around the needle tip in the absence of the jet. A solid metal needle of length 35 mm with an inner diameter of 0.64 mm and outer diameter of 1.0 mm is kept perpendicular to a 50.0-mm-diameter circular metallic collector plate. A potential of 4.8 kV was applied on the needle and the collector plate was grounded. (a) Predicted equipotential lines and electric field lines (with arrows). Most of the potential decays close to the metallic needle and the electric field is 3D in nature near the needle. However, beyond a few radial distances from the needle tip, the equipotential lines are almost uniformly distributed and the electric field is approximately along the axial direction. (b) The variation of the axial electric field $E_{\infty}(z)$.

the axial electric field $E_{\infty}(z)$ which is incorporated in Eq. (4). While the nonuniformity in the external axial electric field is incorporated in the quasi-1D model through $E_{\infty}(z)$, the exact

3D nature of the field near the needle is not accounted for, which may be responsible for the discrepancy in the prediction of the jet radius near the needle.

-
- [1] J. U. Park, M. Hardy, S. J. Kang, K. Barton, K. Adair, C. Y. Lee, M. S. Strano, A. G. Alleyne, J. G. Georgiadis, P. M. Ferreira *et al.*, High-resolution electrohydrodynamic jet printing, *Nat. Mater.* **6**, 782 (2007).
- [2] J. Doshi and D. H. Reneker, Electrospinning process and applications of electrospun fibers, *J. Electrostat.* **35**, 151 (1995).
- [3] A. Barrero and I. G. Loscertales, Micro and nanoparticles via capillary flows, *Annu. Rev. Fluid Mech.* **39**, 89 (2007).
- [4] D. Sun, C. Chang, S. Li, and L. Lin, Near-field electrospinning, *Nano Lett.* **6**, 839 (2006).
- [5] S. H. Ahn, H. J. Lee, and G. H. Kim, Polycaprolactone scaffolds fabricated with an advanced electrohydrodynamic direct-printing method for bone tissue regeneration, *Biomacromolecules* **12**, 4256 (2011).
- [6] J. C. Wang, H. Zheng, M. W. Chang, Z. Ahmad, and J. S. Li, Preparation of active 3D film patches via aligned fiber electrohydrodynamic (EHD) printing, *Sci. Rep.* **7**, 43924 (2017).
- [7] M. S. Onses, E. Sutanto, P. M. Ferreira, A. G. Alleyne, and J. A. Rogers, Mechanisms, capabilities, and applications of high-resolution electrohydrodynamic jet printing, *Small* **11**, 4237 (2015).
- [8] Y. Han and J. Dong, Electrohydrodynamic printing for advanced micro/nanomanufacturing: Current progresses, opportunities, and challenges, *J. Micro Nano-Manuf.* **6**, 040802 (2018).
- [9] X. Chi, X. Zhang, Z. Li, Z. Yuan, L. Zhu, F. Zhang, and J. Yang, Fabrication of microfluidic chips based on an ehd-assisted direct printing method, *Sensors* **20**, 1559 (2020).
- [10] A. K. Singh, R. K. Srivastava, and S. S. Bahga, Regimes of steady jetting in electrohydrodynamic jet printing, *Phys. Rev. Fluids* **7**, 063701 (2022).
- [11] J. Fernández de la Mora, The fluid dynamics of Taylor cones, *Annu. Rev. Fluid Mech.* **39**, 217 (2007).
- [12] J. F. De La Mora and I. G. Loscertales, The current emitted by highly conducting Taylor cones, *J. Fluid Mech.* **260**, 155 (1994).
- [13] M. Cloupeau and B. Prunet Foch, Electrostatic spraying of liquids in cone-jet mode, *J. Electrostat.* **22**, 135 (1989).
- [14] A. Barrero, A. M. Gañán-Calvo, J. Davila, A. Palacio, and E. Gomez-Gonzalez, Low and high reynolds number flows inside Taylor cones, *Phys. Rev. E* **58**, 7309 (1998).
- [15] A. M. Gañán-Calvo, Cone-Jet Analytical Extension of Taylor's Electrostatic Solution and the Asymptotic Universal Scaling Laws in Electrospinning, *Phys. Rev. Lett.* **79**, 217 (1997).
- [16] F. Higuera, Flow rate and electric current emitted by a Taylor cone, *J. Fluid Mech.* **484**, 303 (2003).
- [17] F. Higuera, Stationary viscosity-dominated electrified capillary jets, *J. Fluid Mech.* **558**, 143 (2006).
- [18] A. M. Gañán-Calvo and J. M. Montanero, Revision of capillary cone-jet physics: Electro spray and flow focusing, *Phys. Rev. E* **79**, 066305 (2009).
- [19] S. N. Reznik and E. Zussman, Capillary-dominated electrified jets of a viscous leaky dielectric liquid, *Phys. Rev. E* **81**, 026313 (2010).
- [20] R. T. Collins, J. J. Jones, M. T. Harris, and O. A. Basaran, Electrohydrodynamic tip streaming and emission of charged drops from liquid cones, *Nat. Phys.* **4**, 149 (2008).
- [21] L. K. Lim, J. Hua, C.-H. Wang, and K. A. Smith, Numerical simulation of cone-jet formation in electrohydrodynamic atomization, *AIChE J.* **57**, 57 (2011).
- [22] M. Gamero-Castaño and M. Magnani, Numerical simulation of electrospinning in the cone-jet mode, *J. Fluid Mech.* **859**, 247 (2019).
- [23] A. Ponce-Torres, N. Rebollo-Muñoz, M. Herrada, A. Gañán-Calvo, and J. Montanero, The steady cone-jet mode of

- electrospraying close to the minimum volume stability limit, *J. Fluid Mech.* **857**, 142 (2018).
- [24] H. Dastourani, M. Jahannama, and A. Eslami-Majd, A physical insight into electro-spray process in cone-jet mode: Role of operating parameters, *Int. J. Heat Fluid Flow* **70**, 315 (2018).
- [25] O. Lastow and W. Balachandran, Numerical simulation of electrohydrodynamic (EHD) atomization, *J. Electrostat.* **64**, 850 (2006).
- [26] M. A. Herrada, J. M. López-Herrera, A. M. Gañán-Calvo, E. J. Vega, J. M. Montanero, and S. Popinet, Numerical simulation of electro-spray in the cone-jet mode, *Phys. Rev. E* **86**, 026305 (2012).
- [27] R. Hartman, D. Brunner, D. Camelot, J. Marijnissen, and B. Scarlett, Electrohydrodynamic atomization in the cone-jet mode physical modeling of the liquid cone and jet, *J. Aerosol Sci.* **30**, 823 (1999).
- [28] J. López-Herrera, M. Herrada, J. Montanero, N. Rebollo-Muñoz, and A. Gañán-Calvo, On the validity and applicability of the one-dimensional approximation in cone-jet electro-spray, *J. Aerosol Sci.* **61**, 60 (2013).
- [29] A. M. Gañán-Calvo, On the theory of electrohydrodynamically driven capillary jets, *J. Fluid Mech.* **335**, 165 (1997).
- [30] J. Feng, The stretching of an electrified non-newtonian jet: A model for electrospinning, *Phys. Fluids* **14**, 3912 (2002).
- [31] F. Higuera, Electric current of an electrified jet issuing from a long metallic tube, *J. Fluid Mech.* **675**, 596 (2011).
- [32] J. Melcher and G. Taylor, Electrohydrodynamics: A review of the role of interfacial shear stresses, *Annu. Rev. Fluid Mech.* **1**, 111 (1969).
- [33] D. Saville, Electrohydrodynamics: The Taylor-Melcher leaky dielectric model, *Annu. Rev. Fluid Mech.* **29**, 27 (1997).
- [34] A. M. Gañán-Calvo, The surface charge in electro-spraying: Its nature and its universal scaling laws, *J. Aerosol Sci.* **30**, 863 (1999).
- [35] A. M. Gañán-Calvo, On the general scaling theory for electro-spraying, *J. Fluid Mech.* **507**, 203 (2004).
- [36] J. López-Herrera, P. Riesco-Chueca, and A. Gañán-Calvo, Linear stability analysis of axisymmetric perturbations in imperfectly conducting liquid jets, *Phys. Fluids* **17**, 034106 (2005).
- [37] M. M. Hohman, M. Shin, G. Rutledge, and M. P. Brenner, Electrospinning and electrically forced jets. I. Stability theory, *Phys. Fluids* **13**, 2201 (2001).
- [38] M. M. Hohman, M. Shin, G. Rutledge, and M. P. Brenner, Electrospinning and electrically forced jets. II. Applications, *Phys. Fluids* **13**, 2221 (2001).
- [39] E. Hinch, in *Perturbation Methods* (Cambridge University Press, Cambridge, UK, 1991), p. 43.